

APPLICATION OF LASER VELOCIMETRY TO AIRCRAFT WAKE-VORTEX MEASUREMENTS

Donald L. Ciffone and Kenneth L. Orloff

Ames Research Center

SUMMARY

The theory and use of a laser velocimeter that makes simultaneous measurements of vertical and longitudinal velocities while rapidly scanning a flow field laterally are described, and its direct application to trailing wake-vortex research is discussed. Pertinent measurements of aircraft wake-vortex velocity distributions obtained in a wind tunnel and water towing tank are presented. The utility of the velocimeter to quantitatively assess differences in wake velocity distributions due to wake dissipating devices and span loading changes on the wake-generating model is also demonstrated.

INTRODUCTION

An accurate, quantitative definition of the flow field associated with lift-generated wake vortices behind aircraft is essential if the fluid dynamics of these wakes are to be completely understood. The recent, increasing number of both ground-based and flight experimental investigations of wake-vortex characteristics include flow visualization studies (refs. 1-8), measurements of induced rolling moments on following aircraft (refs. 5 and 9-12), and wake velocity measurements (refs. 13-28). Flow visualization allows the investigator to view the structure of the wake, but leaves him to deduce the quantitative results of the fluid dynamic phenomena observed. Following-aircraft rolling moment measurements allow the investigator to compare wake alleviation concepts, but once again the basic fluid-dynamic phenomena are "explained" deductively. Only a direct measurement of the wake-velocity distributions provides a quantitative understanding of the flow field. These measurements have been attempted using pressure probes (refs. 15 and 16), hot-wire anemometry (refs. 13, 14, 17, 18, and 27), and, more recently, with laser velocimetry (refs. 19-26 and 28). The velocities obtained from a fixed hot wire or

pressure probe are subject to doubt because the probe may interfere with the structure of the vortex. It is questionable whether any mechanical probe can be placed near a small trailing vortex without significantly disturbing the flow. In addition, the meandering motion of vortices in test facilities complicates measurements using stationary probes (refs. 13-17). This vortex motion results in time averaging of velocity measured by a stationary probe, and a consequent loss of measurable detailed structure. The use of a high-speed rotating hot wire (ref. 18) represents one attempt to circumvent this vortex meander problem. Flight measurements have been performed using hot-wire anemometry in which an instrumented probe aircraft follows a generator aircraft to measure wake velocities. These measurements, however, are difficult to interpret and expensive to implement. The laser velocimetry measurement technique does not disturb the flow and has high spatial resolution. In addition, the processed signal from a laser velocimeter is linearly related to the velocity sensed and requires no calibration. The result is a quantitative definition of the flow field which is easy to interpret. These properties of the laser velocimeter make it ideal for studying the fluid dynamics of aircraft trailing wakes.

A laser velocimeter developed at Ames Research Center, which makes simultaneous measurements of vertical and longitudinal velocities while rapidly scanning a flow field laterally, is discussed here. This instrument was developed specifically for wake-vortex measurements. The basic principles of laser velocimetry are reviewed briefly, and some of the more significant results from the application of this instrument to the measurement of aircraft wake-vortex characteristics is presented.

NOMENCLATURE

AR	wing aspect ratio
b	wingspan, m
c	wing reference chord, m
C_L	lift coefficient
r	vortex radius, m
U_∞	free-stream velocity, m/sec

V_x	streamwise velocity, m/sec
V_θ	rotational velocity, m/sec
$V_{\theta_{\max}}$	maximum rotational velocity, m/sec
V_{θ_p}	maximum rotational velocity in plateau region, m/sec
X	downstream distance from trailing edge of wing, m
α	angle of attack, deg
μ	index of refraction
Γ_0	centerline circulation, m^2/sec

Subscripts

B	end of plateau region
P	plateau region

LASER VELOCIMETRY TECHNIQUES

Not long after the introduction of the gas laser in the early 1960's, scientists discovered a way to use the laser to measure the velocity of small micron-sized particles entrained within a gas or liquid. These particles are assumed to move along the streamlines of the flow. If the drag forces acting on the particles dominate their inertia forces, then a measurement of their velocity represents an accurate measurement of the fluid velocity at the location of the particle. This technique has become known as "laser velocimetry," and instruments designed to accomplish this measurement are called "laser velocimeters." The "dual-scatter" or "fringe" mode laser velocimeter has gained widespread acceptance as a result of the ease with which it can be optically aligned and the relatively high signal/noise ratios realized in the measurement of the velocity of particles. In this type of velocimeter, the output beam of a laser is passed through a prism dividing it into two parallel, coherent, beams of equal light intensity, which are then focused through a convex lens to intersect at a point in the flow field where the velocity is to be measured. The velocimeter signal is generated from within the ellipsoidal

volume created by this intersection of the two light beams. This so-called probe volume varies in size from less than 50 microns in diameter in a small optical system to greater than 1 m for a velocimeter designed for atmospheric research. Because of the angle of intersection of the light beams, a pattern of evenly spaced, alternately light and dark interference fringes is formed within the probe volume. These fringes define a set of planes, each normal to the plane defined by the two crossed beams and parallel to the axis of the system (fig. 1). The spacing between the fringes, δ , is given by (ref. 29)

$$\delta = \frac{\lambda_0}{2\mu \sin(\theta/2)} \quad (1)$$

where λ_0 is the vacuum wavelength of the laser light, μ is the index of refraction of the fluid in which the beams intersect, and θ is the included angle between the laser beams. When a particle entrained within the moving fluid traverses the interference pattern, it alternately scatters laser light from the bright fringes at a measurable frequency, f , where

$$f = \frac{V \cos \gamma}{\delta} \quad (2)$$

and γ is the angle at which a particle with velocity V crosses the fringe pattern. Hence measured frequency is proportional to the component of flow velocity normal to the fringe planes and to the sine of the angle of intersection of the laser beams. The sign of the velocity remains undetermined.

Two-Dimensional, Scanning Laser Velocimeter

Figure 2 is a schematic diagram of a laser velocimeter developed by and currently being used at Ames Research Center. This instrument employs the crossed-beam concept described above, but uses the two brightest colors emitted at wavelengths of 4880 and 5145 Å from an argon-ion laser to simultaneously measure two components of the flow velocity. The two distinct colors from the laser makes the most efficient use of available laser power, especially where signal levels are expected to be low. The argon-ion laser was selected not only because it is a source having a multiple line emission spectrum, but also because it provides more response at the photodetector since the photocathodes of the detectors are generally more sensitive in the regions of the spectrum where argon emits radiation than in the longer wavelength region of the spectrum of He Ne lasers. The instrument shown in figure 2 is a crossbeam,

on-axis, backscatter laser velocimeter, where scattered laser light is collected by the same optical system that is used to focus the incident beams. This backscattering mode was selected over a forward-scattering instrument because difficulties in optical alignment are overcome, and not all test facilities have viewing stations on opposite sides of the test section. The two beamsplitters (BS) provide the scanning lens (LN) with two sets of parallel light beams (at 4880 and 5145 Å) orthogonal to each other.

A unique feature of this laser velocimeter is that the probe volume can be rapidly traversed (or scanned) along the optical axis of the system across the flow field while continuously acquiring velocity profiles. The scanning is accomplished by use of a simple "zoom-type" lens combination (LN and LP, see fig. 2). A small change in the position of the lens (LN) moves the probe volume over a much larger distance. The scanning arrangement is essentially a Galilean telescope operating in reverse. As shown in figure 3, the relationship for "scanning sensitivity," dD/dS , to focal length f_{LP} , and scan range, D , can be derived (ref. 30) from simple lens theory:

$$\frac{dD}{dS} = -\left(\frac{D - f_{LP}}{f_{LP}}\right)^2 \quad (3)$$

Figure 4 graphically illustrates the dependence of scanning sensitivity on scan range and focal length. Sensitivities near 30 have been found to be desirable when operating at scan ranges near 2 m. With this sensitivity, a change in lens spacing of 1 cm translates the probe volume 30 cm. The location of the probe volume is obtained from the output of a linear potentiometer that monitors the position of the scanning lens. The limits of the spatial scan are set to encompass the region of interest, and traverses are made continuously at speeds up to 1.6 m/sec with automatic reversal at preset limits. Since the system operates in the "confocal" mode (same optics used for both transmission and reception), the maximum scan rate is limited only by mechanical constraints and the method of signal processing.

The achromatic lens system permits the probe volume from the two colors to be coincident. Backscattered light that contains frequency data for both velocity components is collected by the lens system and is returned parallel to the outgoing laser beams. Mirrors (D and M in fig. 2) then separate the

light into the original colors and they, in turn, are focused onto photomultiplier tubes (PM) for processing.

Signal Processing

The choice of signal processing electronics is based on the flow field to be measured and the expected characteristics of the velocimeter signals (ref. 31). Most of the initial laser studies of vortex wakes at Ames have used spectrum analyzers as the primary signal-processing electronics. These instruments are variable bandwidth filters with selectable sweep rates. The energy content of the signal within the bandwidth is displayed on a cathode ray tube as the filter sweeps through a selected frequency range. Two identical HP 8552/8553 spectrum analyzers operating at processing rates of 15 to 20 sweeps/sec monitored the two components of velocity. From the displayed power spectrum of the frequency (velocity) content of the velocimeter signal, the frequency at which the maximum signal occurs is taken as the average velocity of the flow. For greatest velocity sensitivity, it is desirable to have the range of expected signal frequencies span the acceptance band of the processing electronics. For example, at low velocities, it might be advantageous to increase the signal frequency by increasing the included crossbeam angle (eq. (2)). However, since the f number, $f_{LP/B}$, of the focusing lens, LP, decreases by increasing the included angle,

$$\frac{f_{LP}}{B} = \left[2 \left(\sqrt{1 - \frac{dD}{dS}} + 1 \right) \tan \frac{\theta}{2} \right]^{-1} \quad (4)$$

(under the constraint of low velocity) when larger included angles must be used, the focusing lens must have a low f number. This is illustrated in figure 5, where it is shown that, for a modest beam convergence angle of 6° , a representative scanning sensitivity of 30, and an incident laser light of 5000 \AA , the resulting fringe spacing is 5μ and the required focusing lens f number is 1.5. Spherical aberrations of lenses with low f numbers make optical scanning difficult and must be considered in the overall design and application of the optical system (ref. 30).

Figure 6 is a typical oscillograph trace from a single sweep of the spectrum analyzer during a scan through a vortex. The figure demonstrates how

the frequency information is extracted from the graphical record. The data are recorded on magnetic tape for later review. Typical simultaneously measured velocity distributions through a vortex are presented in figure 7. The streamwise profile provides information related to the drag of the generating model; the rotational distribution provides a measure of the strength of the wake and therefore some indication of the hazard it would present to an encountering aircraft. Several scans were made through the vortex from which mean curves were drawn through the data. Only when the scanning probe volume passes directly through the vortex core are data recorded. For these "core penetrations," the vertical velocity component is the same as the vortex rotational velocity and the longitudinal velocity component is the vortex streamwise velocity.

Spectrum analysis techniques cannot be interpreted without a great deal of difficulty when flows are unsteady or processed when a high level of turbulence is present. As a result, the signal-processing technique described above has recently been replaced by a Raytheon Model 15/55G two-channel frequency tracker to survey the multivortex wake behind a 1.83-m (6-ft) span wind-tunnel model of a Boeing 747 with flaps and landing gear (ref. 31). With the frequency tracker technique, whenever a signal is present above a preset threshold and within the bandwidth of the tracker (100 kHz), the tracker locks on and tracks the signal automatically in less than 3 msec. If the signal should "drop out," a variable time delay "hold" mode (adjustable between 0.1 and 100 msec) keeps the loop locked. After this time, if the signal does not reappear, an automatic "sweep" mode searches for the signal over the entire instrument range (0-15 MHz) in approximately 5 msec. This automatic sweep and lock-on feature of the tracker is important during optical traverses of multiple vortex wakes where there is a continual loss and reappearance of signal as the probe volume scans the wake. When a signal reappears, the signal/noise level can be quite different, and the frequency will often be a considerable distance from the "held" value. The tracker is then required to unlock, search, lock on, and track this new signal. The difference in velocity between the regions far from vortex centers and those near the vortices can produce signal frequencies that vary over a wide range, typically from about 0.5 to 5.0 MHz, in a short period of time. The frequency tracker is able to

track adequately under these conditions since it uses only a single broad frequency range that extends from approximately 0.05 to 15 MHz, with a slew rate capability in excess of 20 MHz/sec.

The data are stored in the core memory of a high-speed data acquisition system (ref. 31) (transient capture device TCD) and can be handled in an on-line fashion, including plotting of fully reduced data or transferring to magnetic tape for storage and playback. Figure 8 shows a TCD record of a scan through the vortices from the inboard edge of the inboard flaps of the Boeing 747 model.

Directional sensitivity is accomplished by rotating the laser system 40° about the optical axis, thus biasing both channels of the velocimeter with a component of the free-stream velocity. The spatially compressed appearance of the wake structure on the right-hand side of the centerline results from the nonlinear scanning speed of the focal point for a constant motion of the scanning lens. Figure 9 shows the final processed (reduced and plotted) data corresponding to figure 8. The data are still being used to obtain relative strengths of the vortices in the wake, turbulence intensity profiles, and to supply initial conditions for theoretical models that will predict the far-field wake characteristics.

Vortex Marking Techniques

Particulate scattering material is introduced into the test media to enhance the signal. For wind-tunnel experiments, smoke is introduced into the diffuser section of the wind tunnel by means of a mineral oil vapor generator. Recirculating the air provides a low-density concentration of the oil vapor throughout the wind tunnel so that velocity data can be gathered at any position in the test section. For water towing-tank studies, polystyrene copolymer latex solution is added to the water to provide scattering. The size distribution of these particles is between 2 and 15 μ . For wind-tunnel experiments, the size of the mineral oil particles is under investigation, but available literature (ref. 32) suggests an upper limit of about 7 microns. For the flow measurements reported here, in which the mean values of the velocity (rather than turbulent fluctuations) are of interest, these particles can be expected

to accurately represent the fluid velocity. Since the particle sizes are not small compared to the wavelength of the incident laser light, their scattering properties are characterized by Mie scattering theory (ref. 33), which states that particle scattering cross section is a complex function of diameter, index of refraction, and the details of the measuring velocimeter (ref. 32). This, however, has not proven to be a liability when measuring the velocity in aircraft trailing wakes with the laser system described.

In wind-tunnel experiments, the centers of wake vortices are often visible because the core is seen as a dark region that lacks white smoke. As a result, reflections from the laser beams are significantly dimmer at the very center of the vortex because of the scarcity of light-scattering material. This makes it possible to observe visually when a traverse passes through the center of the vortex, and the event is marked on a separate recording channel of the magnetic tape. These "core penetration" events are transferred onto the oscillograph record from which the data are reduced. A small amount of core motion is acceptable when the probe volume of the velocimeter is well outside the vortex core region and the velocity gradients are low. However, acceptable traverses are limited to core penetrations in which no vortex movement is evident.

In the water tow-tank experiments, the vortex centerlines were marked by generating a thin sheet of air bubbles across the tank 1.5 m upstream (toward the starting end) of the test section location of the laser. The streamwise velocity defect in the vortex core region then acted in such a way as to drag some of these bubbles toward the passing airfoil; the radial pressure gradient associated with the rotational flow centered the bubbles in single file, producing a fine string of bubbles along the vortex centerline. As the vortex pair moved vertically in the tank, the laser system was also moved manually to keep the optical axis aligned with the vortex centerline. When the vortices could not be readily marked and visually located, the region of interest in the wake was mapped out by making continuous lateral traverses through the wake at different elevations.

A new technique of vortex marking in the water-tow tank (developed specifically for flow visualization studies, refs. 6 and 8) involves injecting

fluorescent dyes directly into the vortices from the wake-generating model and illuminating them with a system of lights (fig. 10). A separate, high-speed scan - short focal length - laser system with a high scan sensitivity is being developed for use with this flow visualization system to quantitatively assess the flow fields of multiple vortex wakes.

VORTEX-VELOCITY MEASUREMENTS

The scanning, two-color, dual-beam, backscatter; argon-ion laser velocimeter described previously has been used to measure the vertical and streamwise velocity components in wakes containing vortices. The measurements have been made both in a wind tunnel (refs. 12-21, 24, and 31) and a water-towing facility (refs. 22, 23, 25, and 26). The need for a rapid scanning instrument differed for the two facilities. For the wind tunnel, the trailing vortices are fully established but may wander in a random manner. The center of the vortex does not remain stationary within the test section because large-scale eddies are convected through the wind tunnel. Hence the vortex must be traversed during a time which is short compared to the movement of the vortex. As discussed previously, the optical scanning is performed in a direction normal to the tunnel centerline. This is shown schematically in figure 11 for a semispan model and photographically in figure 12 for a 1.83-m (6-ft) span model of the Boeing 747. The model was mounted in an inverted position to minimize the interference of the support strut with the wake.

For the towing tank, rapid scanning at a given measurement station is required because of the time-dependent nature of the trailing vortices as the wing model is towed through the tank. The flow field does not have perturbations of the vortex velocity about a mean steady-state velocity, but rather a decaying shear flow. In this case, a meaningful time history of the vortex requires that the time for an optical traversal be short compared with vortex decay time, so that a mean "age" can be assigned to each measured profile. As the vortex pair moves in the tank due to its mutual influence, it is necessary that the velocimeter moves vertically while scanning to keep the optical axis aligned with the vortex centerline. Spanwise continuous traversals of the

probe volume through the near-side wake are made with the automatic scan reversal set to encompass the area of interest (figs. 13 and 14).

Wind-Tunnel Test Results

The first application of the laser velocimeter to measure the streamwise and rotational velocity distributions in vortices was to a square-tipped, 0.457-m chord, 1.218-m semispan wing mounted in the Ames 7- by 10-Foot Wind Tunnel (ref. 20). The airfoil section was an NACA 0015 and the planform was rectangular with no twist. Detailed velocity profiles were obtained at a scanning rate of 15 cm/sec (fig. 7) and were found to be in general agreement with data (ref. 18) obtained with a hot-wire probe mounted on the end of a rapidly rotating boom. This velocity information provides for a comparative evaluation of vortex alleviation schemes, as was demonstrated for a dissipator panel mounted on the rectangular wing. A square panel (4 percent of the semispan, 11 percent of the wing chord) was installed at the wing tip at the 1/4-chord position. A comparison of the measured velocity distributions showed a reduction in maximum rotational velocity and the development of a large streamwise velocity defect due to the panel.

The reduction in maximum rotational velocity, $V_{\theta_{\max}}$, as a function of downstream distance is summarized in figure 15, together with the results obtained from the rapidly moving hot-wire data (ref. 18) of a geometrically similar configuration in the Ames 40- by 80-Foot Wind Tunnel at 55 chord lengths downstream. ($V_{\theta_{\max}}$ was assumed to be the average maximum of the two peaks of the rotational velocity distribution (fig. 7).) From these results, it appears that the mechanism that alleviates the vortex develops with increasing downstream distance.

The need for experimental velocity distributions in the wakes of wings more representative of present-day transport aircraft was the rationale for the second series of wind-tunnel tests (ref. 21). Velocity profiles were obtained in the wake of a Convair-990 semispan wing (fig. 11). The effects of configuration buildup (including flaps, flow-through nacelles, and antishock bodies) and wingspan loading changes due to flap deflection and angle of attack were investigated. The effect of wingspan loading on the wake was

evident when a factor of 2 reduction in $V_{\theta\max}$ was obtained at a constant lift coefficient by deploying the flaps and reducing the angle of attack.

Water Tow-Tank Test Results

The wind-tunnel data on vortex streamwise and rotational velocity profiles are limited by the physical lengths of the wind-tunnel test sections. What was lacking were measured velocity profiles that described the wake structure from several span lengths to hundreds of span lengths. An integration of the measured rotational velocities across the wingspan of encountering aircraft would then yield an evaluation of the magnitude of the rolling moment induced by a vortex at more realistic downstream locations. Therefore, tests were performed in the University of California's water tow-tank facility at Richmond, California. In this method of testing, the model is towed underwater (figs. 13 and 14), generating a continuous wake that decays with time at each longitudinal point of the test gallery (fig. 10). The test time ends when the vortex structure is altered by interference from boundaries of the water or the passage through the test section of internal vortex waves, which arise from starting or stopping the model at the ends of the towing range.

Effect of wing planform on wake - The first sequence of tests (ref. 22) was designed to investigate the effects of wing planform on wake characteristics and to compare the results with near-field wake data obtained in wind tunnels with similar airfoils. The three planforms tested are described in table I. Typical data obtained which illustrate the effects of wing planform on vortex rotational velocity profiles are presented in figures 16 and 17, at 20 and 100 span lengths, respectively.

The diamond wing planform resulted in a lower concentration of vorticity in the core and diminished circumferential velocities in the adjacent regions. Both features are desirable in alleviating the wake hazard potential. At 100 span lengths downstream, the velocity profiles were found to be quite similar, indicating that the effect of wing planform is no longer discernible.

The maximum rotational velocities (obtained by averaging the two peak values of velocity) identified two characteristic flow regions for their dependence on downstream distance (figs. 18 and 19). The first, a "plateau"

region, with little change in maximum rotational velocity, extended from wake rollup to downstream distances as great as 100 span lengths, depending on span loading. This plateau is followed by a decay region in which the maximum rotational velocity decreases with downstream distance at a rate nominally proportional to the inverse half-power. This plateau did not come as a complete surprise since its existence is suggested in the turbulent shear-flow calculations of Donaldson (ref. 34). There was concern as to whether the initiation of the velocity decay was a real flow phenomenon or a consequence of starting and stopping waves. This possibility was explored experimentally and analytically and is discussed at length in reference 22. It was concluded that the test results were not affected by motion waves. The results indicate that inviscid vortex structure calculations should be applicable to downstream distances as great as 45 spans for rectangular wings at lower lift coefficients. A demonstration of the nearly inviscid nature of the flow field in the plateau region was made by Rossow (ref. 35), who used an inverse Betz technique to predict the span loading from the measured velocity profiles in this region.

Figure 18 presents the effect of span-load change due to angle-of-attack change for the rectangular wing planform. Also shown are results obtained from geometrically similar wings tested in the Ames 40- by 80-Foot and 7- by 10-Foot Wind Tunnels (refs. 18 and 20). The agreement is seen to be reasonably good. Figure 19 shows span-loading effects due to wing planform at a common angle of attack of 5° . The data have been normalized by dimensionless circulation to eliminate effects due to differences in lift coefficient and aspect ratio of the wings. The vertical bars indicate the end of the plateau region.

A time history of streamwise velocity profiles for the rectangular wing at 8° angle of attack is presented in figure 20. These results characterize the radial diffusion of the streamwise velocity defect in the decay region. A profile obtained in the near field (ref. 20) ($X/b = 0.38$) has been included to emphasize the initial concentration of streamwise momentum. The diffusion of the streamwise component of velocity can be traced in this way and its maximum value along the axis can be extracted and used in subsequent decay considerations.

Figure 21 shows how the maximum vortex-core streamwise velocity (in the towing direction) for the rectangular wing decreases with downstream distance

and angle of attack. The wind-tunnel data of references 14 and 20 and the water-tank data of references 36 and 37 are shown for comparison. The present data indicate a far-field maximum streamwise velocity decay that is inversely proportional to downstream distance to approximately the $1/4$ power. Also shown in the figure are the streamwise velocity defect and rate of decay on the vortex centerline as computed (ref. 23) from the laminar theory of reference 38. The comparison is remarkably good and improves with decreasing angle of attack — believed to be a consequence of the approximation that $V_x \ll U_\infty$ in the analysis.

Effect of flap deflections on wake - In a second sequence of tests in the water tank (ref. 25), the swept-wing planform was fitted with seven flap segments on each half span. The flaps were used to achieve additional desired wingspan loadings. Four different span loadings at a lift coefficient of 0.70 were selected for investigation: (1) the wing with no flaps deflected? (2) a typical landing configuration, (3) a configuration tailored to reduce the gradient in the loading at the wingtip, and (4) a configuration with flaps deflected alternately $\pm 15^\circ$ in an attempt to create multiple spanwise spanload gradients (sawtooth effect in the spanload distribution). These configurations are illustrated in figure 22. The flap schedules and test angles of attack to produce a common lift coefficient of 0.70 for all configurations are listed in table II.

A comparison of the effect of span loading on vortex rotational velocity distributions due to various combinations of flap deflections is presented in figures 23 and 24 at 25 and 95 span lengths downstream. All the data are at a common lift coefficient of 0.70. Much like the diamond wing planform, the tailored configuration yields lower rotational velocities in the core and adjacent regions and has a more diffuse velocity profile. However, once again, at 95 span lengths downstream in the decay region, the rotational velocity profiles are quite similar. At span lengths of 95, the dependence of the velocity profile on wingspan loading has lost most of its significance.

The downstream dependence of maximum rotational velocity for these configurations is summarized in figure 25. Although the limited amount of data precludes a positive identification of a plateau region for these flapped

configurations, the data suggest its presence. The decay region is readily apparent. Although a plateau region could never really be identified for the sawtooth configuration, the wake did eventually roll up (at 30 span lengths) and achieve rotational velocities almost comparable to the clean and landing configurations. At a lift coefficient of 0.7, there is little difference in the downstream characteristics of the maximum rotational velocities in the wake of the clean wing or the landing configuration. The results obtained with the tailored configuration are much like those obtained with the diamond wing planform. The maximum wake tangential velocities are less than half those of the other configurations, and the plateau region extends to 80 span lengths. Once again, this long plateau is instrumental in reducing the initial large differences in maximum rotary velocities to insignificant differences in the far wake.

A comparison of the measured radial distribution of streamwise velocity in the core of the vortices behind these swept-wing configurations at 75 span lengths downstream is presented in figure 26. The results show a streamwise velocity defect toward the model for all configurations.

Plateau velocity correlation - A correlation function based on the self-similar turbulent decay of a line vortex has been developed (ref. 39) and utilized to substantiate the validity of using ground-based scale model data to predict high Reynolds number flight results. It was found that if the downstream dependence of vortex maximum rotational velocity is presented as a vortex velocity scaling parameter, $V_1 b / \Gamma_0 AR$, versus a distance scaling parameter, $(X/b) (\Gamma_0 / U_\infty b) (AR)^2 f(\Gamma_0 / \nu)$, the scale model and flight data collapse to a single curve. Presented in figure 27 are the results obtained when these scaling parameters are used to plot vortex maximum rotational velocity in the plateau region versus a corresponding downstream duration of this region obtained from the towing tank data presented previously (ref. 26). The line faired through the experimental points has a slope of -1, which implies the following inverse proportionality between the plateau velocity and extent of the plateau region:

$$\left(\frac{V_\theta}{U_\infty}\right)_p \left(\frac{X}{b}\right)_B = \frac{47}{AR f(\Gamma_0/\nu)} \quad (5)$$

The Reynolds number parameter, $f(\Gamma_0/\nu)$, was developed in reference 39 and is a function of vortex Reynolds number, $\Gamma_0/\nu = (\Gamma_0/U_\infty b) \text{Re}(b)$. For $\Gamma_0/\nu \geq 3 \times 10^5$, $f(\Gamma_0/\nu) = 1$. Hence, for all flight conditions, $f(\Gamma_0/\nu) = 1$, and for most ground-based tests (including the water-tank tests of refs. 22 and 25), $f(\Gamma_0/\nu)$ is of order 1.

Use of equation (5) and a $-1/2$ decay region downstream dependence of vortex maximum rotational velocity allows near-field wake velocity measurements in the plateau region (i.e., wind-tunnel data) to be used to estimate subsequent far-field vortex characteristics. The lines through the data in figures 18, 19, and 25 predict the downstream variation of maximum rotational velocity with this approach. The vertical bars indicate the predicted end of the plateau region. The predictions and measurements are seen to be in good agreement.

CONCLUDING REMARKS

The theory and use of a laser velocimeter with high-speed spatial scanning capability has been described and its direct application to trailing wake vortex research has been presented. The scanning feature of this instrument minimizes the difficulties in velocity measurement due to what has been termed "vortex meander." Accurate vortex definition is achieved and the data are repeatable and consistent with other experimental results.

Measurements have been made of changes in wake rotational and streamwise velocity components due to span-loading changes of the wake-generating model. The results identified two characteristic flow regions for the dependence of vortex maximum rotational velocity on downstream distance. The first, a region of constant velocity, can extend from wake rollup to 80 span lengths downstream behind the generating wing, depending on span loading and angle of attack. This is followed by a decay region where $V_{\theta_{\max}}$ varies approximately as $(X/b)^{-1/2}$. This implies that inviscid vortex structure calculations should be applicable to distances as great as 80 span lengths downstream for certain wing configurations.

It was shown that tailoring the wingspan loading by either planform shape or flap deflection (to reduce wing-tip vorticity by unloading the outboard sections of the wing) is equally effective in reducing the wake rotational velocities by factors of 2, broadening the vortex core, and extending the plateau region to 80 span lengths.

An orderly wake rollup was delayed to 40 span lengths downstream by introducing multiple vortices along the wingspan with alternate up-down flap deflections. These multiple vortices interacted with each other, resulting in large excursions in the wake and linking to form irregular loops. A plateau region was never achieved for this configuration.

A correlation of the water-tank results relates the magnitude of vortex maximum rotational velocity in the plateau region to the downstream extent of this region. With this knowledge, near-field wake velocity measurements in the plateau region (i.e., wind-tunnel results) can be used to estimate the far-field vortex characteristics.

REFERENCES

1. Garodz, L. J.; Lawrence, D.; and Miller, N.: The Measurement of the Boeing 727 Trailing Vortex System Using the Tower Fly-By Technique, Rept. FAA-RD-74-90, Aug. 1974.
2. Tymczyszyn, J. J.; and Barber, M. R.: A Review of Recent Wake Vortex Flight Tests. 18th Annual Symposium of Society of Experimental Test Pilots, Los Angeles, Calif., Sept. 26, 1974.
3. Barber, M. R.; Kurkowski, L. J.; Garodz, L. J.; Robinson, G. H.; Smith, H. J.; Jacobsen, R. A.; Stinnett, G. W.; McMurtry, T. C.; Tymczyszyn, J. J.; Devereaux, R. L.; and Bolster, A. J.: Flight Test Investigation of the Vortex Wake Characteristics Behind a Boeing 727 During Two-Segment and Normal ILS Approaches, NASA TM X-62,398 and FAA-NA-75-151, Jan. 1975.
4. Huffaker, R. M.; Jeffreys, H. B.; Weaver, E. A.; Bilbro, J. W.; Craig, G. D.; George, R. W.; Gleason, E. H.; Marrero, P. J.; Reinbolt, E. J.; and Shirey, J. E.: Development of a Laser Doppler System for the

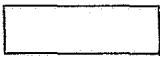
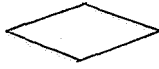

- Detection, Tracking and Measurement of Aircraft Wake Vortices, Rept. **FAA-RD-74-213**, March 1975.
5. Corsiglia, V. R.; Rossow, V. J.; and Ciffone, D. L.: Experimental Study of the Effect of Span Loading on Aircraft Wakes, NASA TM **X-62,431**, 1975.
 6. Ciffone, D. L.; and Lonzo, C., Jr.: Flow Visualization of Vortex Interactions in Multiple Vortex Wakes Behind Aircraft, NASA TM **X-62,459**, 1975.
 7. Patterson, J. C., Jr.; and Jordan, F. L., Jr.: A Static-Air Flow Visualization Method to Obtain a Time History of the Lift-Induced Vortex and Circulation, NASA TM **X-72,769**, 1975.
 8. Ciffone, D. L.: Vortex Interactions in Multiple Vortex Wakes Behind Aircraft, AIAA Preprint **76-72**, Jan. 1976.
 9. Croom, D. R.: Low-Speed Wind-Tunnel Investigation of Various Segments of Flight Speed-Brake Spoilers as Trailing-Vortex Hazard-Alleviation Devices on a Transport Aircraft Model, NASA TN (to be published).
 10. Patterson, J. C., Jr.; and Jordan, F. L., Jr.: An Investigation of the Increase in Vortex Induced Rolling Moment Associated with Landing Gear Wake, NASA TM **X-72,786**, 1975.
 11. Dunham, E. R., Jr.: Model Tests of Various Vortex Dissipation Techniques in a Water Towing Tank, NASA TN (to be published).
 12. Smith, H. J.: A Flight Test Investigation of the Rolling Moments Induced on a T-37B Airplane in the Wake of a **B-747** Airplane, NASA TM **X-56,031**, 1975.
 13. Chigier, N. A.; and Corsiglia, V. R.: Tip Vortices-Velocity Distributions, NASA TM **X-62,087**, 1971.
 14. Chigier, N. A.; and Corsiglia, V. R.: Wind-Tunnel Studies of Wing Wake Turbulence, J. Aircraft, vol. **9**, no. **12**, Dec. 1972, pp. **820-825**.
 15. Mason, W. H.; and Marchman, J. F., 111: Farfield Structure of an Aircraft Trailing Vortex, Including Effects of Mass Injection, NASA CR-62,078, 1972.

16. Logan, A. H.: Vortex Velocity Distributions at Large Downstream Distances, *J. Aircraft*, vol. 8, no. 11, Nov. 1971, p. 930.
17. Corsiglia, V. R.; Jacobsen, R. A.; and Chigier, N. A.: An Experimental Investigation of Trailing Vortices Behind a Wing with a Vortex Dissipator, *Aircraft Wake Turbulence and Its Detection*, 1st ed., Plenum Press, New York, 1971, pp. 229-242.
18. Corsiglia, V. R.; Schwind, R. G.; and Chigier, N. A.: Rapid Scanning Three-Dimensional Hot Wire Anemometer Surveys of Wing Tip Vortices, *J. Aircraft*, vol. 10, no. 12, Dec. 1973, p. 762.
19. Grant, G. R.; and Orloff, K. L.: A Two-Color Dual-Beam Backscatter Laser Doppler Velocimeter, *Appl. Optics*, vol. 12, Dec. 1973, p. 2913.
20. Orloff, K. L.; and Grant, G. R.: The Application of Laser Doppler Velocimetry to Trailing Vortex Definition and Alleviation, NASA TM X-62,243, 1973.
21. Ciffone, D. L.; Orloff, K. L.; and Grant, G. R.: Laser Doppler Velocimeter Investigation of Trailing Vortice Behind a Semispan Swept Wing in a Landing Configuration, NASA TM X-62,294, 1973.
22. Orloff, K. L.; Ciffone, D. L.; and Lorincz, D.: Airfoil Wake Vortex Characteristics in the Far Field, NASA TM X-62,318, 1973.
23. Ciffone, D. L.; and Orloff, K. L.: Axial Flow Measurements in Trailing Vortices, *AIAA J.*, vol. 12, Aug. 1974, pp. 1154-1155.
24. Orloff, K. L.; and Ciffone, D. L.: Vortex Measurements Behind a Swept-Wing Transport Model, *J. Aircraft*, vol. 11, no. 6, June 1974, pp. 362-364.
25. Ciffone, D. L.; and Orloff, K. L.: Far-Field Wake-Vortex Characteristics of Wings, *J. Aircraft*, vol. 12, no. 5, May 1975, pp. 464-470.
26. Ciffone, D. L.: Correlation for Estimating Vortex Rotational Velocity Downstream Dependence, *J. Aircraft*, vol. 11, no. 11, Nov. 1974, pp. 716-717.

27. Jacobsen, R. A.: Hot Wire Anemometry for In-Flight Measurement of Aircraft Wake Vortices, 5th Annual Society of Flight Test Engineers Symposium, Anaheim, Calif., Aug. 8-10, 1974.
28. Baker, G. R.; Barker, S. J.; Bofah, K. K.; and Saffman, P. G.: Laser Anemometer Measurements of Trailing Vortices in Water, *J. Fluid Mech.*, vol. 65, pt. 2, 1974, pp. 325-336.
29. Bossel, H. H.; Hiller, W. J.; and Meier, G. E. A.: Noise-Cancelling Signal Difference Method for Optical Velocity Measurements, Rept. 7/71, Max-Planck-Institut für Strömungsforschung Göttingen, 1971.
30. Orloff, K. L.; and Biggers, J. C.: Laser Velocimeter Measurement of Developing and Periodic Flows, International Workshop on Laser Velocimetry, Purdue Univ., March 1974.
31. Orloff, K. L.; Corsiglia, V. R.; Biggers, J. C.; and Ekstedt, T. W.: The Application of Laser Velocimeter Signal Processing Electronics to Complex Aerodynamic Flows, LDA-Symposium, Technical University of Denmark, Lyngby, Denmark, 1975.
32. Orloff, K. L.; Myer, F. C.; Mikas, M. F.; and Phillips, J. R.: Limitations on the Use of Laser Velocimeter Signals for Particle Sizing, International Workshop on Laser Velocimetry, Purdue Univ., Oct. 1975.
33. Grant, G. R.; and Donaldson, R. W.: A Laser Velocity Measurement System for High-Temperature Wind Tunnels, NASA TM X-1976, 1970.
34. Donaldson, C. DuP.: Calculation of Turbulent Shear Flows for Atmospheric and Vortex Motions, *AIAA J.*, vol. 10, Jan. 1972, pp. 4-12.
35. Rossow, V. J.: Prediction of Span Loading from Measured Wake-Vortex Structures - An Inverse Betz Method, *J. Aircraft*, vol. 12, no. 7, July 1975, pp. 626-628.
36. Olsen, J. H.: Results of Trailing Vortex Studies In a Towing Tank, in *Aircraft Wake Turbulence and Its Detection*, edited by J. H. Olsen, A. Goldberg, and M. Rogers, Plenum, New York, 1971, p. 455.
37. Lezius, D. K.: Study of the Far Wake Vortex Field Generated by a Rectangular Airfoil in a Water Tank, NASA TM X-62,274, 1973.

38. Moore, D. W.; and Saffman, P. G.: Axial Flow in Laminar Trailing Vortices, Proc. Roy. Soc. (London), Sec. A, vol. 333, 1973, pp. 491-508.
39. Inverson, J. D.: Correlation of Turbulent Trailing Vortex Decay Data, J. Aircraft (to be published),

TABLE I.- MODEL GEOMETRY

	Rectangular wing	Diamond wing	Swept wing
Planform			
Span	61 cm (24 in.)	61 cm (24 in.)	61 cm (24 in.)
Reference chord	11.43 cm (4.5 in.)	11.43 cm (4.5 in.)	10.41 cm (4.1 in.)
Aspect ratio	5.33	5.33	5.85
Root chord	11.43 cm (4.5 in.)	22.86 cm (9.0 in.)	18.21 cm (7.17 in.)
Leading edge sweep	0°	20.6'	38.6°
Taper ratio	1.0	0	0.25
Section root	NACA 0015	NACA 0015	NACA 0011-64 (modified)
Tip	NACA 0015	NACA 0015	NACA 0008-64 (modified)

Configuration	Semispan flap settings, ^a deg							C _L	α, deg
	(Inboard)			(Outboard)					
Clean	0/	0/	0/	0/	0/	0/	0	0.70	6.8
Landing	20/20/	20/	0/	0/	0/	0/	0	.70	3.4
Tailored	10/10/	0/-	10/-	15/-	20/-	30		.70	7.5
Sawtooth	-15/15/-	15/	-15/	15/-	15/	-15		.70	9.2

^aDownward deflections are' positive.

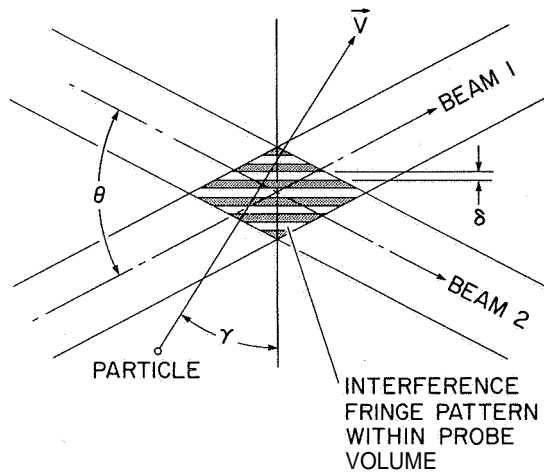


Figure 1.- Geometry of crossbeam system.

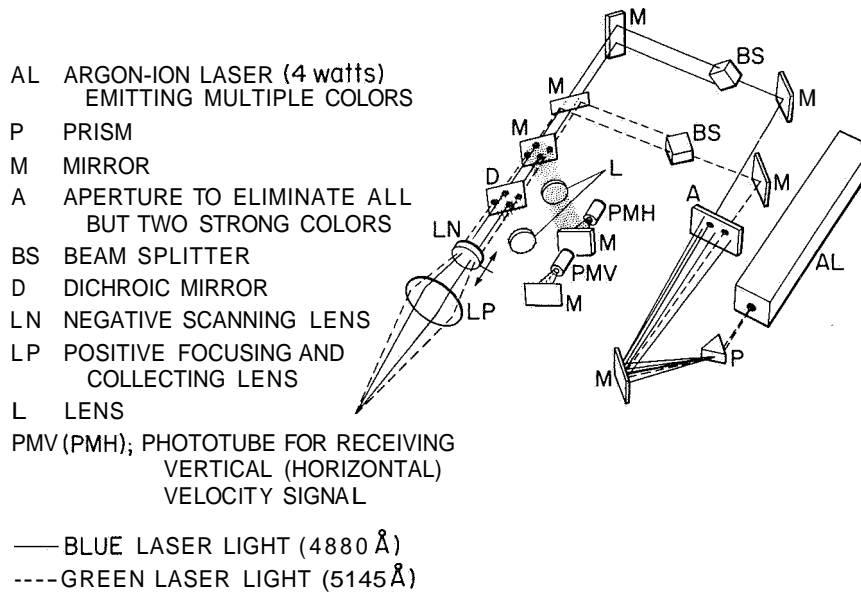


Figure 2.- Schematic representation of the Ames two-dimensional, backscatter, scanning, laser velocimeter (ref. 20).

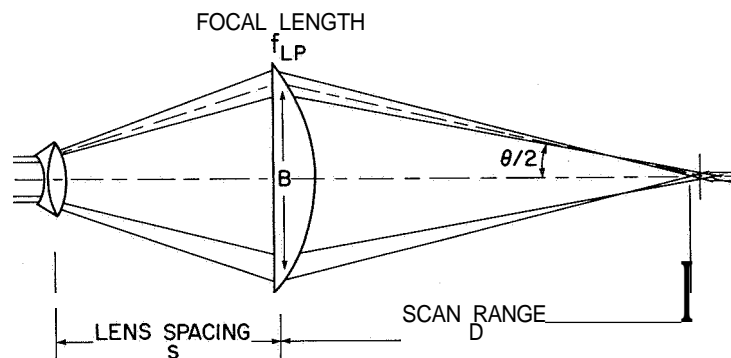


Figure 3.- Scanning lens system used for both transmission and reception (ref. 30).

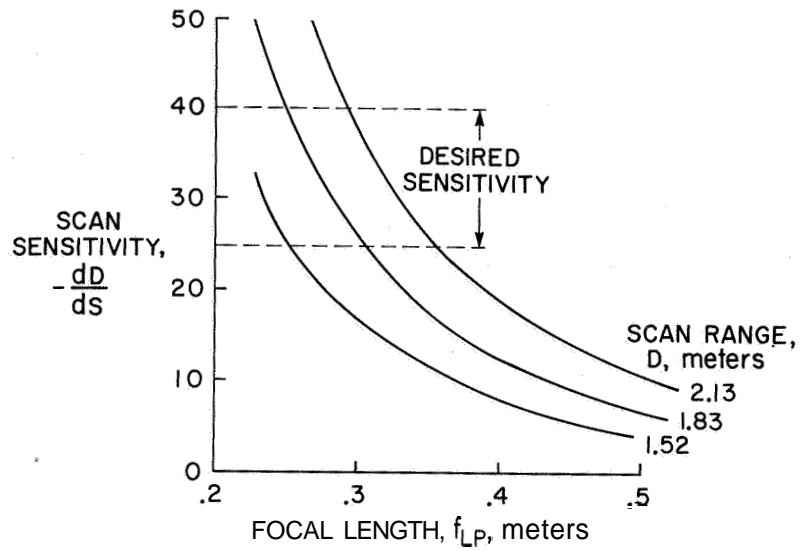


Figure 4.- Variation of scan sensitivity with focal length of focusing lens for several scan distances (ref. 30).

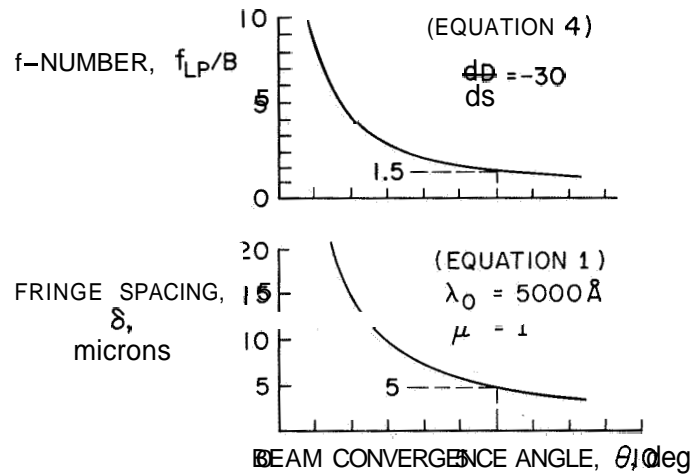


Figure 5.- Dependence of fringe spacing and required f number with beam convergence angle (ref. 30).

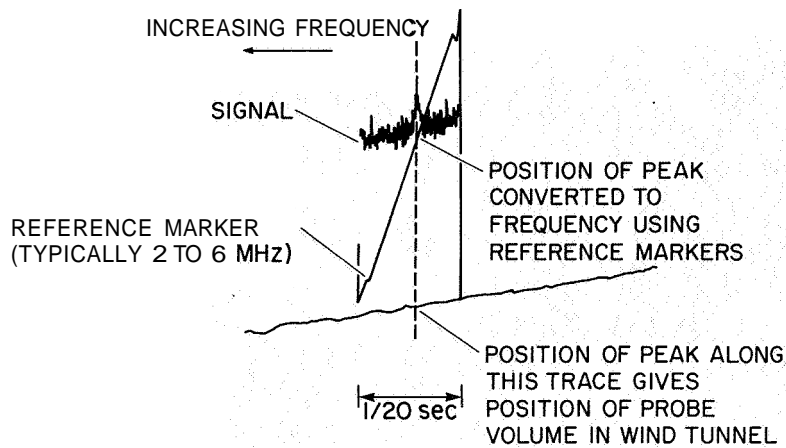


Figure 6.- Oscillograph trace of spectrum analyzer and lens carriage linear potentiometer outputs (ref. 20).

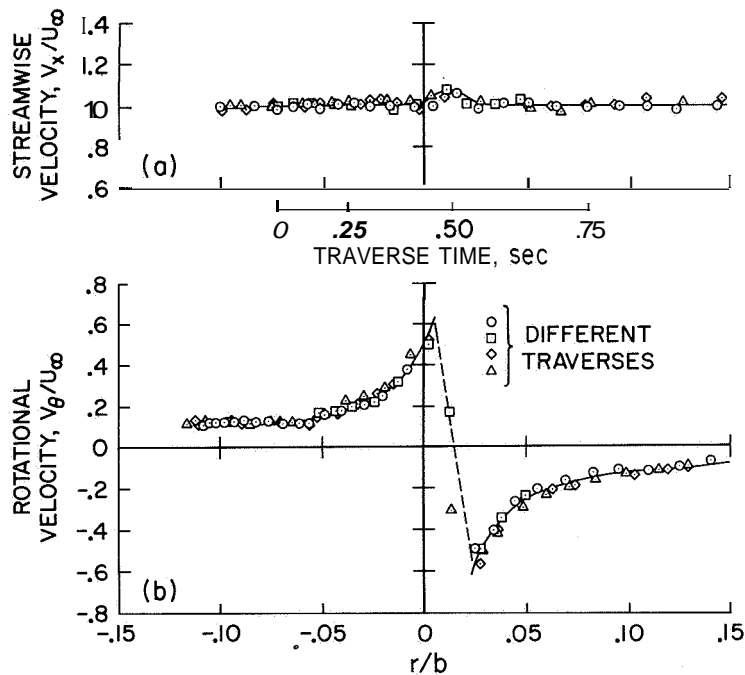


Figure 7.- Velocity distributions through wing-tip vortex of a semispan, square-tipped, rectangular wing with NACA 0015 airfoil; (a) streamwise velocity and (b) rotational velocity. $\alpha = 11.1^\circ$, $U_\infty = 22.8$ m/sec, $b = 2.44$ m, $X/c = 7.0$ (ref. 20).

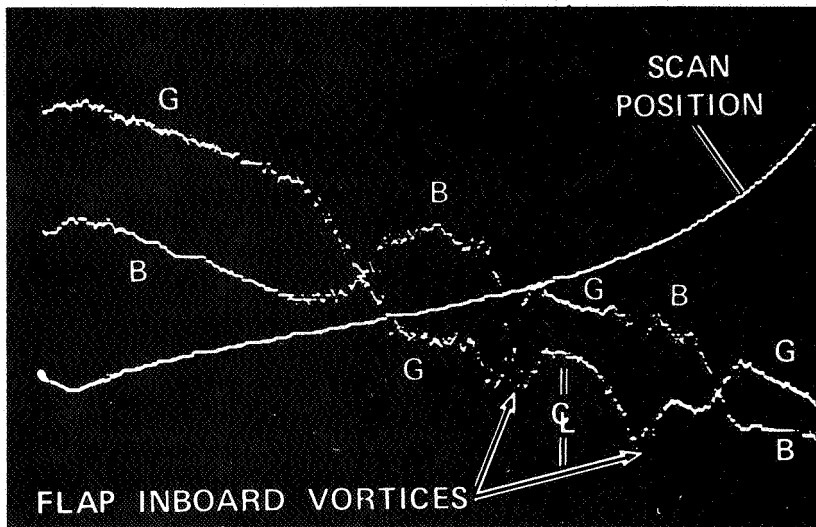


Figure 8.- Boeing 747 wake TCD record showing scan position of focal point, centerline of wind tunnel, and tracker outputs corresponding to the 4880 Å (B) and 5145 Å (G) channels of the velocimeter. This survey is through the vortex pair from the inboard edges of the inboard flaps. Inboard flaps deflected 30°, outboard flaps retracted? gear down; $\alpha = 8^\circ$, $U_\infty = 13.5$ m/sec, $b = 1.8$ m, $X/b = 1.5$ (ref. 31).

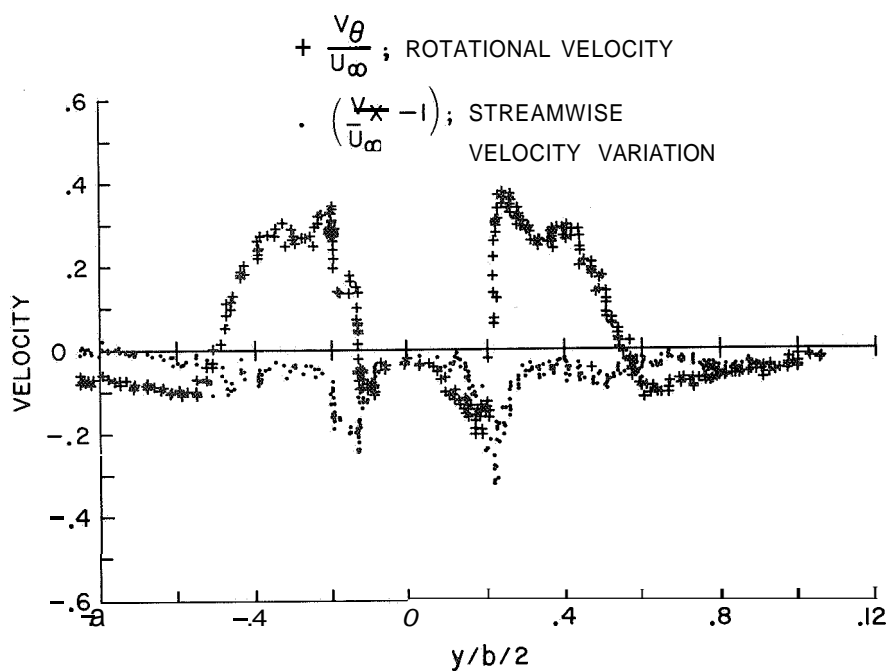


Figure 9.- Processed and plotted data from TCD record in figure 8 (ref. 31).

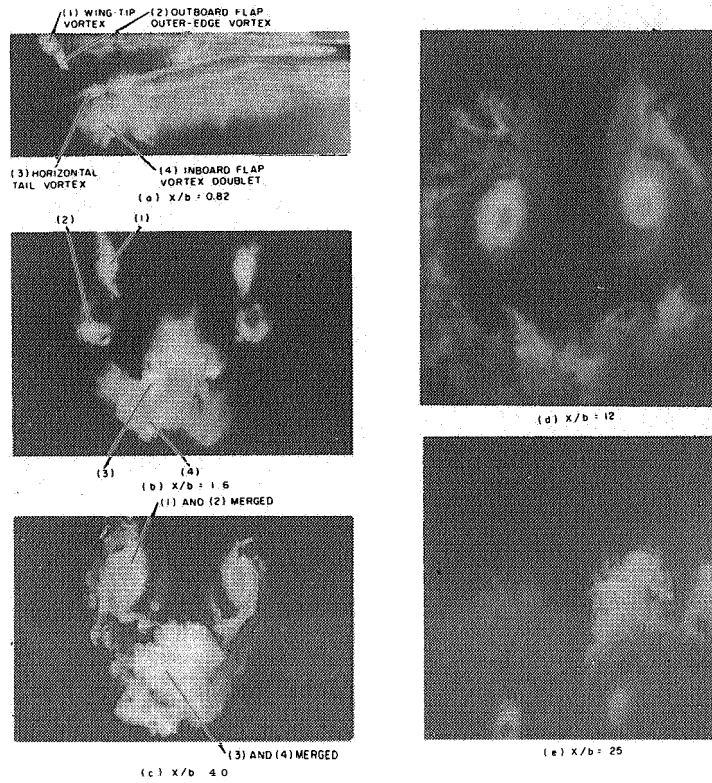


Figure 10.- Cross section of wake in light sheet; Boeing 747 landing configuration; $\alpha = 2.9^\circ$ (ref. 8).

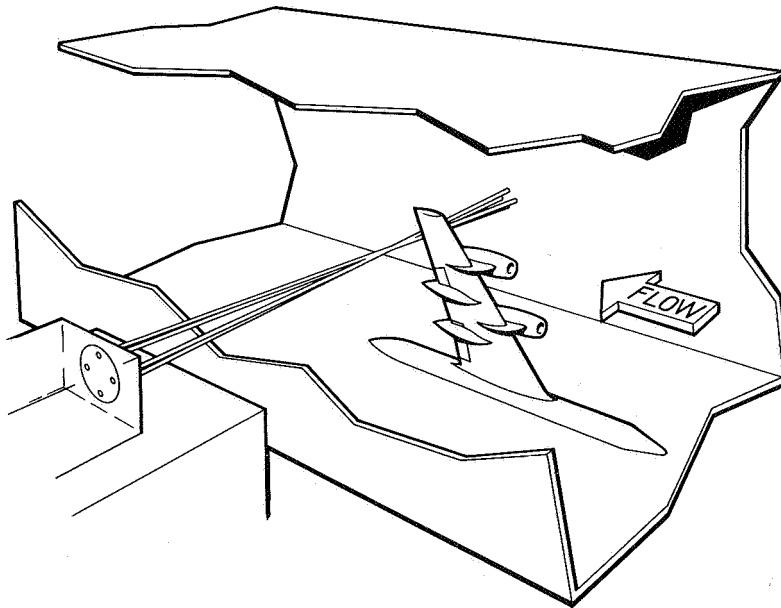


Figure 11.- Installation schematic drawing of semispan model in the Ames 7- by 10-Foot Wind Tunnel and location of scanning velocimeter (ref. 21).

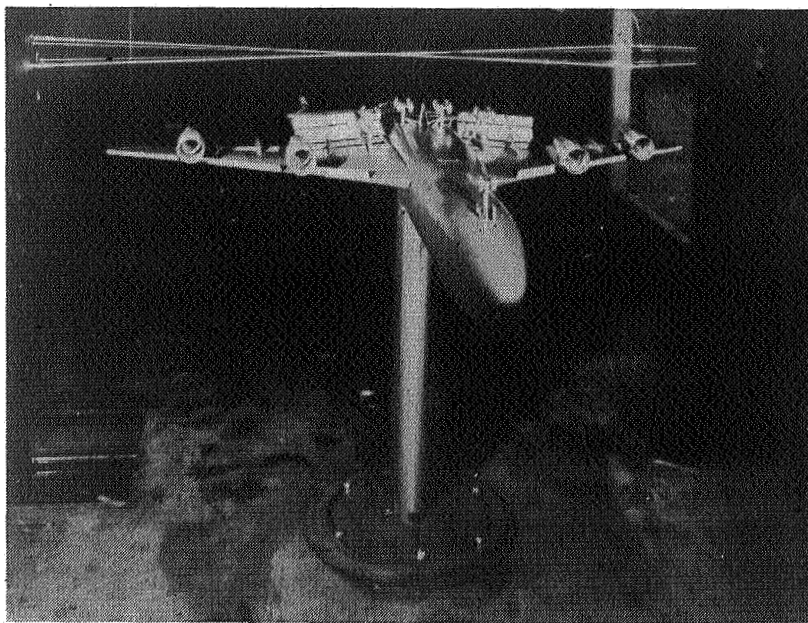


Figure 12.- Boeing 747 model installed in the Ames 7- by 10-Foot Wind Tunnel. Velocimeter scans behind the model at 1.5 wingspans (3 m) aft of the wing trailing edge (ref. 31).

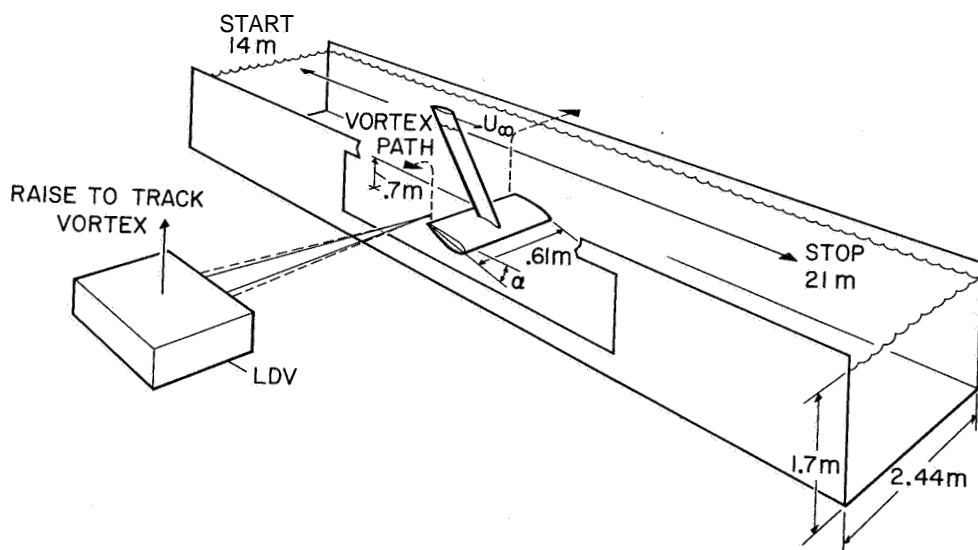


Figure 13.- Installation schematic drawing of model in water tow tank and vortex-tracking technique (ref. 22).

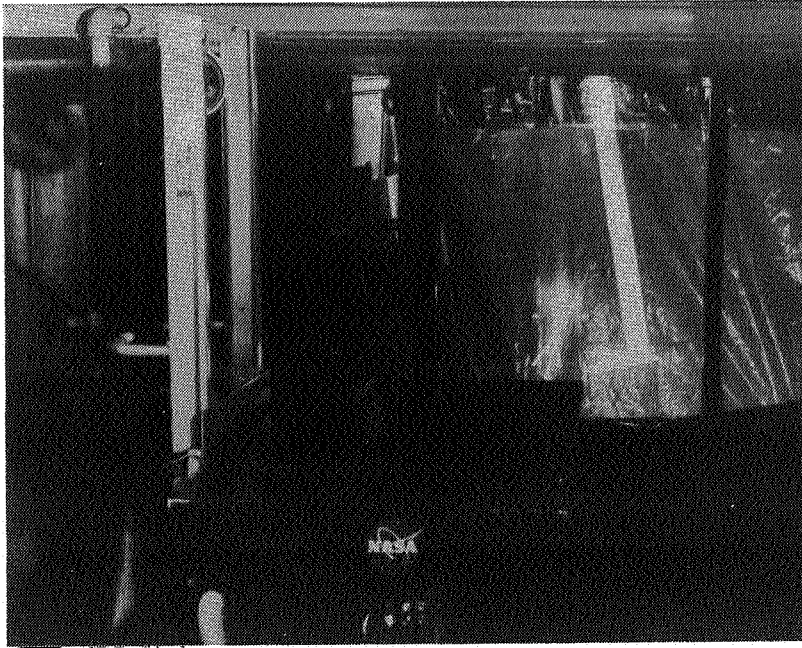


Figure 14.- Installation photograph, swept-wing model in test section of University of California water tow tank (ref. 25).

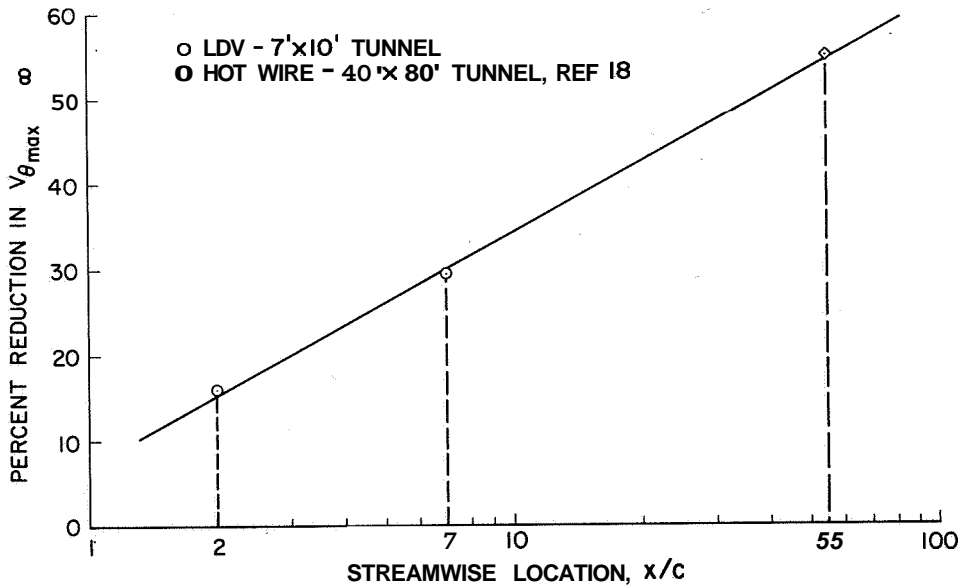


Figure 15.- Streamwise development of dissipator alleviation technique, $\alpha = 12^\circ$ (ref. 20).

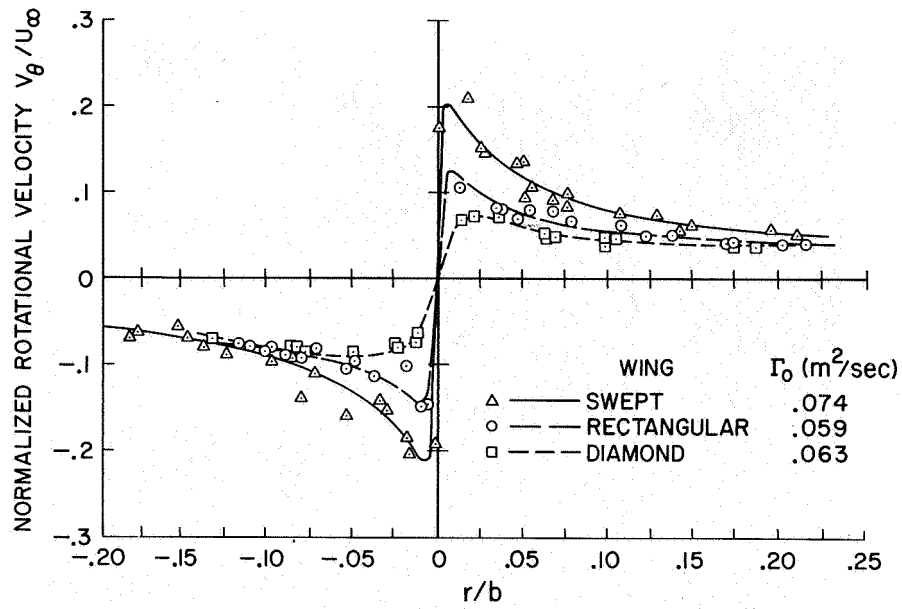


Figure 16.- Radial distribution of rotational velocity for different wing planforms at $X/b = 20$, $a = 5^\circ$, $U_\infty = 2.07$ m/sec (ref. 22).

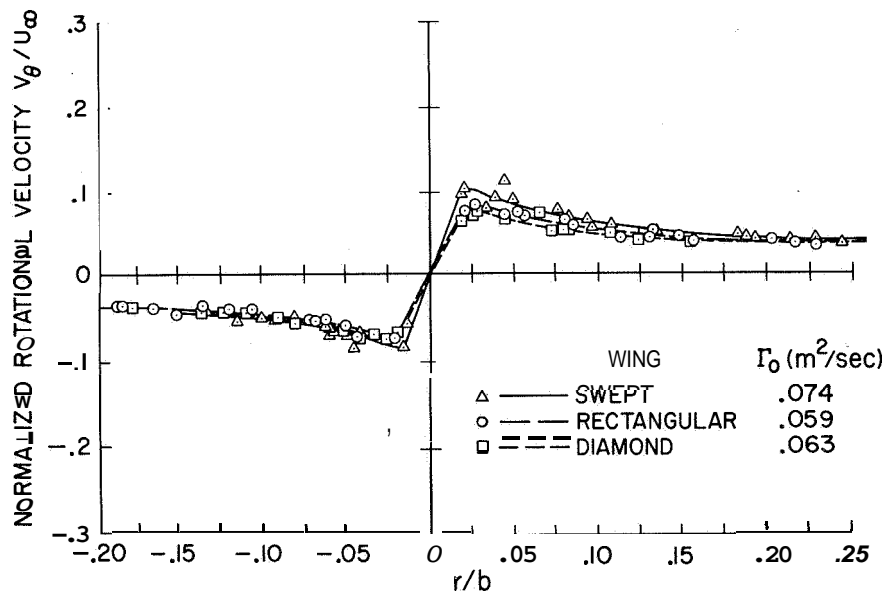


Figure 17.- Radial distribution of rotational velocity for different wing planforms at $X/b = 100$, $a = 5^\circ$, $U_\infty = 2.07$ m/sec (ref. 22).

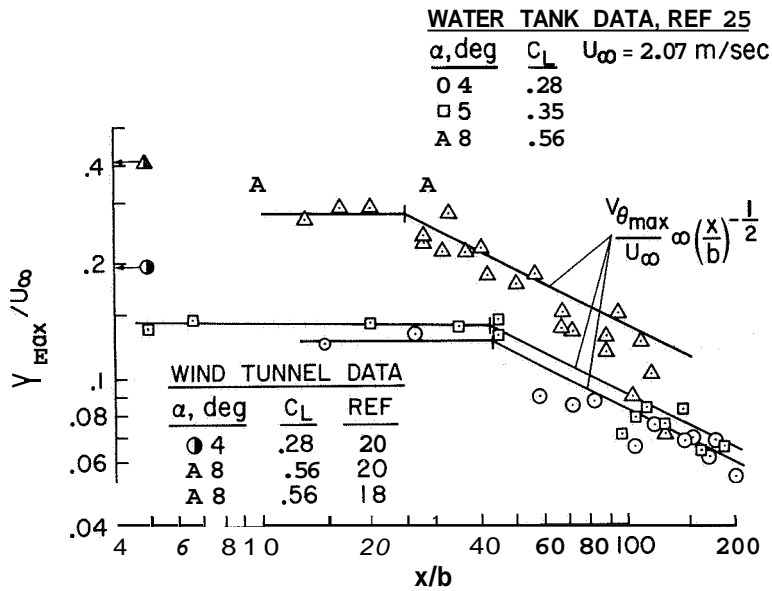


Figure 18.- Dependence of measured maximum rotational velocity on downstream distance and angle of attack, rectangular wing (ref. 26).

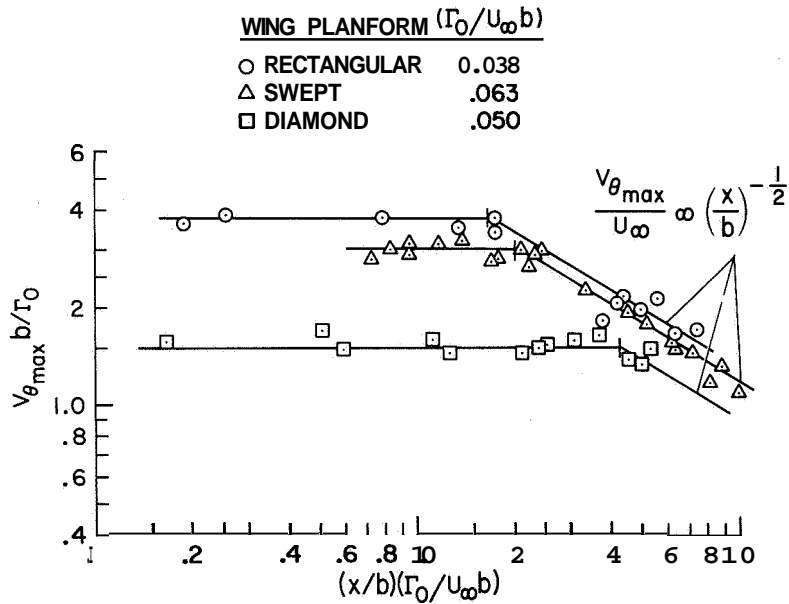


Figure 19.- Dependence of measured maximum rotational velocity on downstream distance and wing planform. Water tank data, $U_\infty = 2.07$ m/sec, $\alpha = 5^\circ$ (refs. 25 and 26).

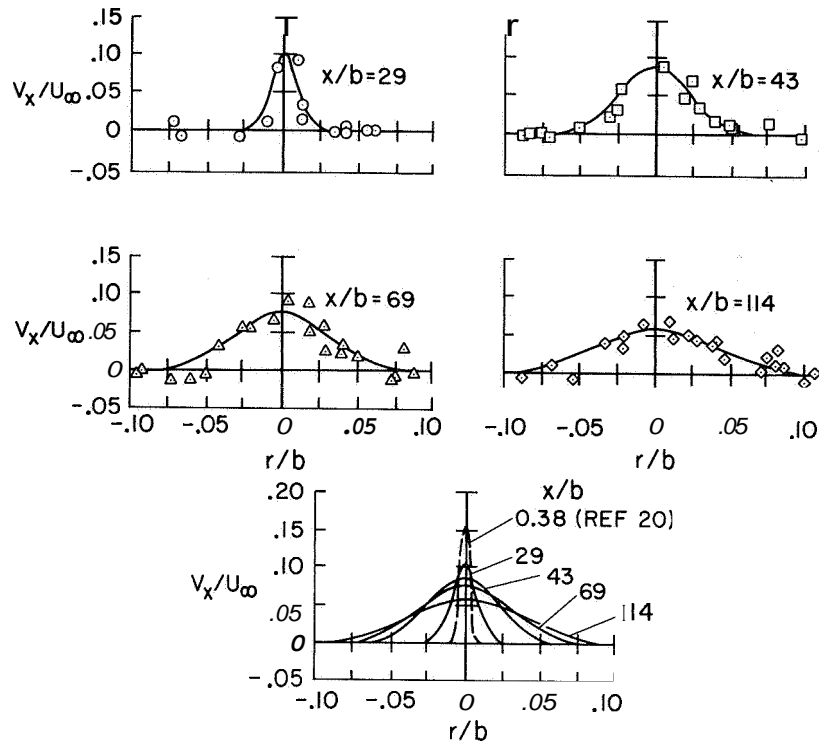


Figure 20.- Rectangular wing streamwise velocity-profile time histories,
 $U_{\infty} = 2.07$ m/sec, $\alpha = 8^{\circ}$. (ref. 25).

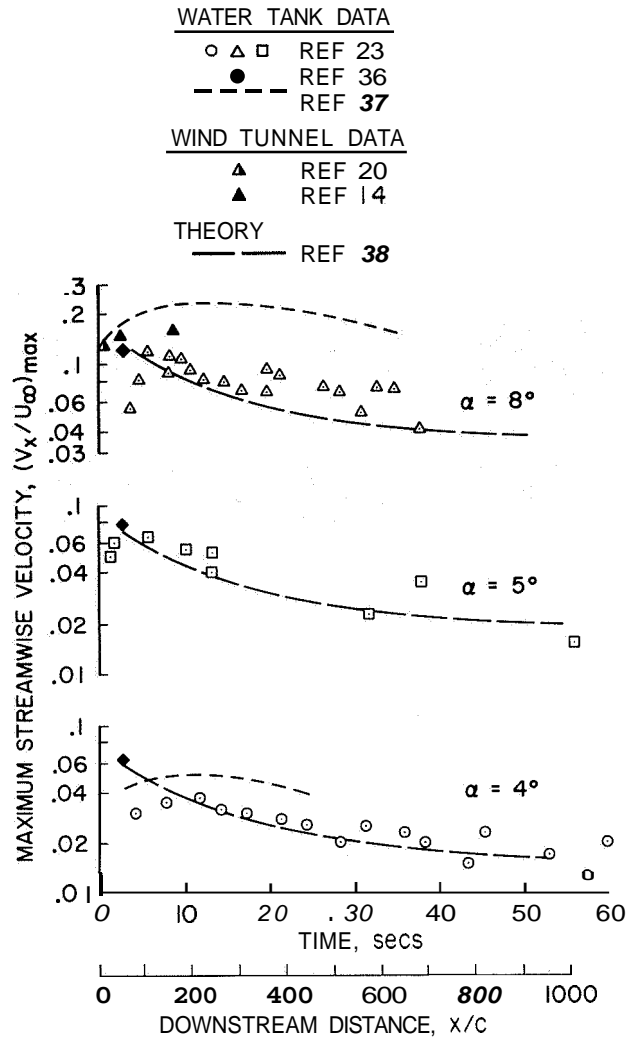


Figure 21.- Dependence of measured maximum streamwise velocity on downstream distance and angle of attack; rectangular planform; $U_\infty = 2.07$ m/sec (ref. 23).

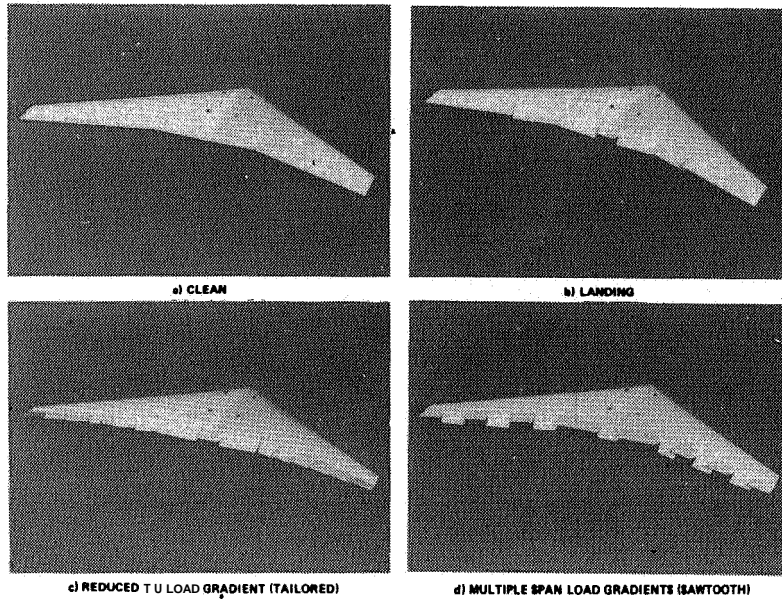


Figure 22.- Swept-wing model test configurations: (a) clean configuration, (b) landing configuration, (c) tailored configuration, (d) sawtooth configuration (ref. 25).

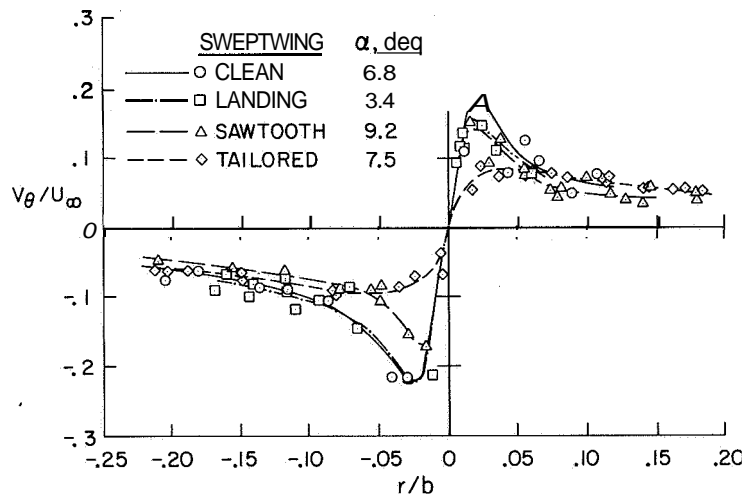


Figure 23.- Comparison of swept-wing configuration rotational velocity profiles; $U_{\infty} = 2.07 \text{ m/sec}$, $C_L = 0.7$, $x/b = 25$ (ref. 25).

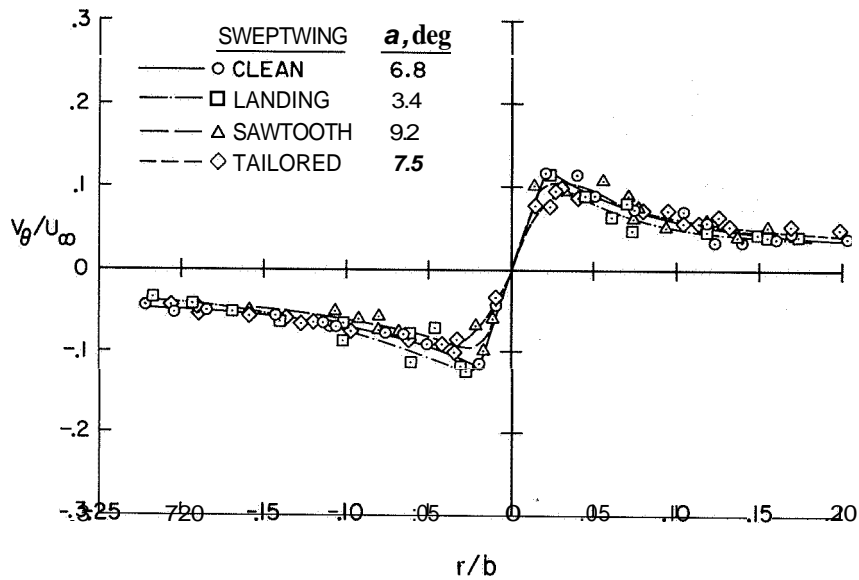


Figure 24.- Comparison of swept-wing configuration rotational velocity profiles;
 $U_\infty = 2.07$ m/sec, $C_L = 0.7$, $X/b = 95$ (ref. 25).

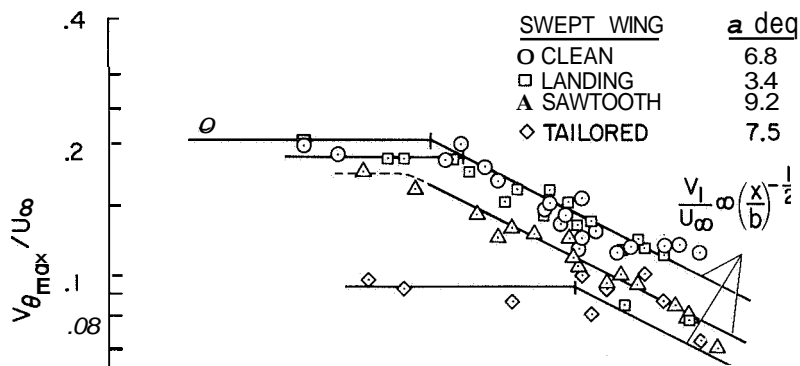


Figure 25.- Dependence of measured maximum rotational velocity on downstream distance and wingspan loading. Water tank data, $U_\infty = 2.07$ m/sec, $C_L = 0.7$ (refs. 25 and 26).

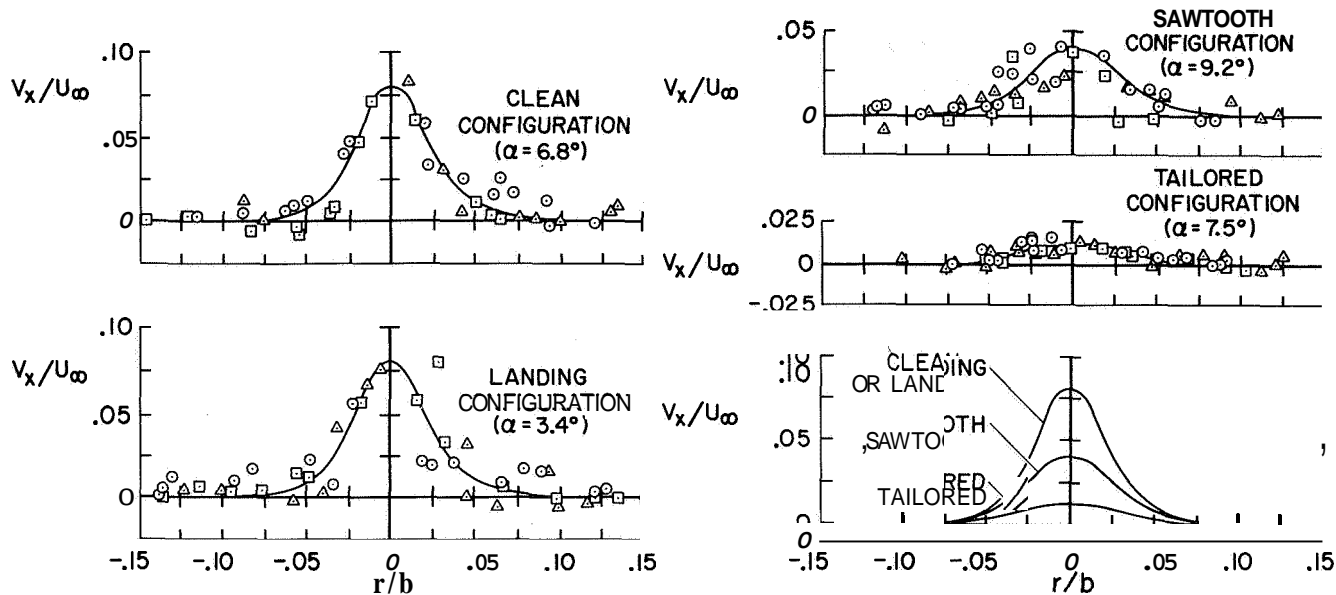


Figure 26.- Comparison of swept-wing configuration streamwise velocity profiles; $U_\infty = 2.07$ m/sec, $C_L = 0.7$, $x/b = 75$ (ref. 25).

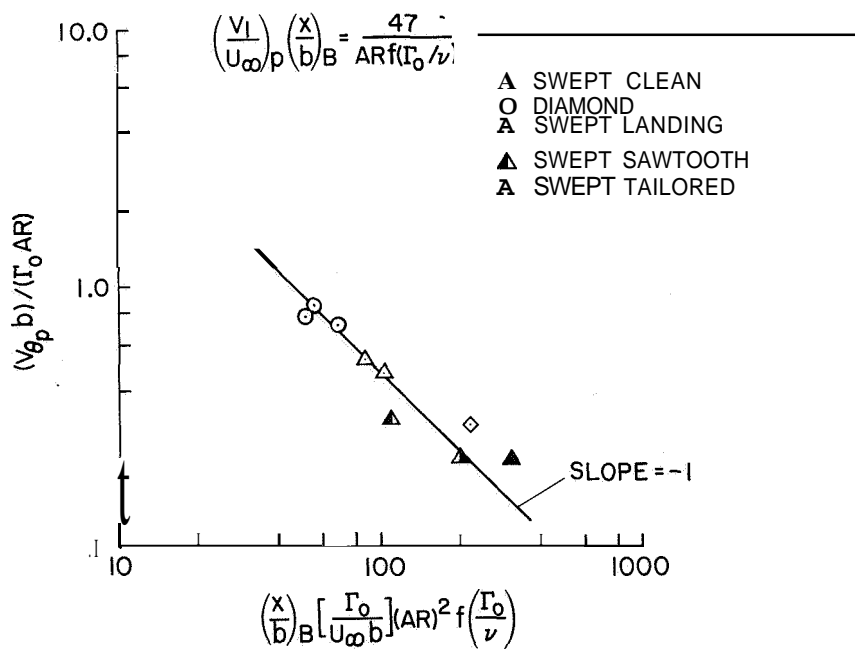


Figure 27.- Correlation of vortex maximum rotational velocity in plateau region to downstream duration of this region (ref. 26).